SAND99-0255J

A Finite Element Method for Free-Surface Flows of Incompressible Fluids in Three Dimensions, Part II: Dynamic Wetting Lines

T. A. Baer*, R. A. Cairncross, P. R. Schunk*, R. R. Rao*, P. A. Sackinger***

***Sandia National Laboratories**
Albuquerque NM 87185

****Drexel University**
Chemical Engineering Department
Philadelphia, PA 19104

DISCLAIMER

Abstract

To date, few reserchers have solved three-dimensional free-surface problems with dynamic wetting lines. This paper extends the free-surface finite element method described in a companion paper[1] to handle dynamic wetting. A generalization of the technique used in two dimensional modeling to circumvent double-valued velocities at the wetting line, the so-called kinematic paradox, is presented for a wetting line in three dimensions. This approach requires the fluid velocity normal to the contact line to be zero, the fluid velocity tangent to the contact line to be equal to the tangential component of web velocity, and the fluid velocity into the web to be zero. In addition, slip is allowed in a narrow strip along the substrate surface near the dynamic contact line. For realistic wetting-line motion, a contact angle which varies with wetting speed is required because contact lines in three dimensions typically advance or recede a different rates depending upon location and/or have both advancing and receding portions. The theory is applied to capillary rise of static fluid in a corner, the initial motion of a Newtonian droplet down an inclined plane, and extrusion of a Newtonian fluid from a nozzle onto a moving substrate. The extrusion results are compared to experimental visualization.

KEYWORDS: three dimensional, free surface, contact lines, wetting lines, simulation, finite element method, pseudo-solid mesh motion.

Introduction

Even with a powerful numerical method of predicting free and moving boundary problems in three dimensions[1], modeling practical problems with dynamic contact lines poses many outstanding challenges. These contact lines represent the curve in three-dimensional space where liquid, gas, and solid meet. Wetting problems involve dynamic contact lines in which the liquid is displacing the gas, or vice versa, along the solid surface. The approaches for treating dynamic contact lines in two dimensions are not easily extended to three dimensions, both conceptually and practically.

Wetting phenomena are often categorized as *static* or *dynamic*. Dynamic wetting involves the relative motion of a fluid/solid/gas contact line and a solid which is *forced* by a large relative velocity (i.e. plunging a substrate rapidly into a quiescent pool of liquid) or *spontaneous* by the propensity of liquid/gas/solid system to lower its free energy by advancing or receding on a surface. Contact lines within all of these classes are common in manufacturing processes like continuous liquid film coating (forced wetting), soldering and brazing (forced and spontaneous), flow in porous media (forced and spontaneous displacement), and many other technologically important areas. For decades researchers have attempted to contrive continuum models that are useful to engineering analysis which simulate the true physics; however, all of the models have implementation aspects that have been simplified to two dimensions where a true contact line becomes a point. At that point, the theoretical treatment of wetting is categorically static or dynamic, a classification which greatly simplifies implementation in a model. In three-dimensions it is often the case to have both of these extremes active along a single contact line, and even worse the local wetting regime will span a large range of local capillary numbers, from static to dynamic. In this paper we present generalizations of what is well-established as acceptable *ad hoc* procedures for modeling static and dynamic contact lines in two dimensions so that they can be applied in three dimensional situations.

The physical differences between static and dynamic wetting regimes are important to the approach taken here. Static wetting lines at which two fluids (usually gas and liquid) meet at fixed curve on a solid boundary are nicely described from a hydrodynamic viewpoint as a nearly stagnant region at which the fluid mechanics are unimportant, i.e., typically trivial Dirichlet conditions on the velocity components suffice. A static contact angle can be considered a thermodynamic property[2], although it may be a complex function of the underlying chemical makeup and structure of the surface which often lead to hysterisis effects. Dynamic wetting lines, at which one fluid displaces the other along the solid boundary, are another matter. A dynamic wetting angle is not a thermodynamic property, but the result of a complex interplay of a variety of nonequilibrium processes. First and foremost are the local hydrodynamics around an advancing or receding wetting line. Those hydrodynamics include both the fluid mechanics in the displacing fluid and in the receding fluid. Then there are the surface tension-related phenomena on the fluid-fluid interface near the contact line. The usual static wetting forces are present at low

capillary numbers, and there is the possibility of surface tension gradients due to the presence of surface active species or temperature gradients. Finally, somewhere and somehow near the three-phase line some mechanism equivalent to fluid slip on the solid surface must be operative in order to relieve the otherwise singular stress that would result (the so-called rolling-motion regime is an exception[3]).

The mathematical condition that is used most often in computational analysis of free surface flows for determining the surface position is the so-called kinematic surface condition[1]. Local surface kinematics near a dynamic contact line as governed by this condition have important implications on speed of the liquid parcels on the surface and those adhered to the substrate around a dynamic contact line. Without evaporation, the kinematic condition demands that the air-liquid surface be a material stream surface right up to the contact line. If the liquid cannot penetrate the solid, as is usually the case, an additional condition of impenetrability must be applied. For both of these conditions to be true, the liquid velocity immediately at the wetting line and the velocity of the wetting line itself must be the same. For steady flow in two-dimensions this implies zero velocity. However, the velocity at the contact line must also be the substrate velocity if no-slip is enforced to include the contact line. This situation of double-valued velocities has been termed the "kinematic paradox", as coined by Kistler[4], and is a situation that demands some liquid slip at the moving solid surface. Only for the case of a 180 degree contact angle is it possible to satisfy all conditions at the contact line simultaneously. This situation is often referred to as the rolling motion condition[3]. For angles other than 180 degrees, researchers have adopted several approaches in finite element or finite difference applications as discussed below.

The most common approach restricts the analysis to conventional continuum theory at macroscopic length scales. It removes the multivalued velocity at the wetting line by ad hoc boundary conditions that allow slip at the line (i.e. the liquid velocity at the wetting line is the same as that of the line) and partial slip nearby, and prescribes a contact angle that is supposed to represent an apparent dyamic contact angle of the sort observed in experiments, possibly taken from an empirical correlation. This approach permits computed predicition of realistic wetting processes[5]. There are many pitfalls to this approach that should be considered (see Christodoulou, Kistler and Schunk[6]), but nonetheless it is this approach we extend here to three dimensions. It is true for

instance that the mesh refinement required to resolve this set of conditions is exceedingly large, especially in three dimensions, and this casts some doubt to the accuracy of the angle being applied, as the microscopic angle may be drastically different.

Other approaches have overcome the need to specify perfect slip at the putative wetting line by exploiting the weak form of the Galerkin weighted residual equations[4] or by taking advantage of collapsed elements which give multiple coincident nodes at the contact line[7, 8]. Although these techniques work well in two dimensions, they undermine severely the mesh convergence of the flow field around the contact line and are impractical in three dimensions due to difficulties in mesh generation and manipulation along a three dimensional contact line (perhaps the double-valued velocity at the contact line achieved with collapsing elements is a possibility).

Two other approaches are worthy of mention. The first adheres to the use of standard *ad hoc* boundary conditions at a contact line, i.e. prescribed contact angle and local slip flow, but imposes a sub-microscopic static angle and systematically refines the mesh to permit a local analysis[9,10,11]. This procedure works well for small capillary number, but is limited at larger ones. This limitation is unfortunate as the approach shows promise in three dimensions. The second approach seeks to resolve the submicrosopic physics of dynamic wetting. It incorporates a refined model for the local air displacement mechanism right into a macrosopic computation, and thereby attempts to provide realistic boundary conditions for the maroscopic flow. Some have attempted this approach at realistic conditions[12] but the challenges of dealing with meshing distortion in three dimensions are enormous.

To date there have been several significant published work in three dimensions that are important to mention here, as they set an important precedent. Dimitrakopoulos and Higdon[13] employed boundary element formulations to determine the configuration of a three-dimensional droplet just prior to motion. An experimental work by Extrand and Kumagai[14] considered a similar topic. Two related papers[15,16], sought perturbation solutions to finding the shape of a droplet down an inclined plane with and without hysteresis in the contact angle model. Finally, a recent theoretical paper by Schwartz and Eley[17] presents a technique for simulating the motion of very small droplets on heterogenous surfaces where surface tension forces dominate.

In the first section below we begin with a generalization of the so-called kinematic paradox to three-dimensional contact line motion. Although obvious in hindsight, the implementation requires a variable contact angle model. We formulate a linear relation between the local contact angle and the local wetting speed, or local capillary number. This model or the equivalent is necessary in nearly every situation as the local wetting speed often varies greatly along a moving contact line, even diminshing to a point at which the line becomes static relative to the moving surface. The next section discusses implementing these concepts and models into a Galerkin finite element code. Finally we present three examples to demonstrate the new model. The first involves the capillary rise of fluid in a corner geometry, the second , the motion of a drop down an inclined surface, and the third the laydown of a liquid bead on a moving substrate. The important feature of the last two problems is that the wetting regimes vary from static to dynamic along the contact line.

Physical Theory of a Wetting Lines in 3D

The Kinematic Paradox in 2D

In two dimensions the contact line is represented as a single point where the free surface intersects a moving substrate boundary. The kinematic condition imposed on the free surface imposes a purely tangential flow velocity along it. The impenetrability and no slip constraints associated with the moving substrate, impose a fluid velocity at the contact line that is parallel to the substrate boundary. For any contact angle other than $180°$, these two requirements are incompatible and require that two velocities exist at the contact line in order to satisfy both simultaneously. This incompatibility is often referred to as the "kinematic paradox." It is a paradox in the sense that a fluid particle arriving at the wetting line will be faced with two possible velocities and hence two possible future trajectories. Because conventional models of fluid flow do not typically consider this possibility, the result is a singularity in fluid stress when an attempt is made to apply them at the wetting line.

To resolve this paradox, it is often suggested that there are wetting forces locally near the contact line (on the subgrid scale) that induce a spreading velocity of the fluid which, at steady state, exactly cancels the motion of the substrate and results in zero velocity of the fluid in the

fixed frame of reference *when viewed on the scale of the problem.* In effect, this model of wetting phenomena does not attempt to resolve the intricate details of the wetting zone region, but instead recognizes that from a sufficient distance the motion of the fluid at the contact line has little influence elsewhere and therefore can be considered stationary. However, since the fluid at the wetting line now has a velocity different from the substrate, it is necessary to also include a region near the wetting line where slip is permitted. The next section extends this notion to a three dimensional wetting line.

Generalization to a Contact Line in Three Dimensions

Figure 1 shows a typical free surface geometry near the wetting line. The web surface has a normal vector, $\boldsymbol{n}_w$, and is moving at velocity $\boldsymbol{u}_w$. The free surface intercepts the substrate at a dynamic contact line with unit normal and tangent vectors, $\boldsymbol{n}_{cl}$ and $\boldsymbol{t}_{cl}$, both of which are orthogonal to $\boldsymbol{n}_w$, *i.e.* in the plane of the substrate.

To circumvent the kinematic paradox in three dimensions, we recognize that, as in two dimensions, slipping of the fluid at the contact line must be permitted; we define the wetting velocity, u_{wet} to be the normal component of the fluid velocity at the contact line *relative to the substrate:*

$$u_{wet} = \boldsymbol{n}_{cl} \bullet (\boldsymbol{u} - \boldsymbol{u}_w). \tag{1}$$

We assume that the wetting velocity in three dimensions is the same as the wetting velocity under similar conditions in two dimensions and that curvature effects are negligible along the contact line. Because the contact line is curved in three dimensions the wetting speed must vary along the contact line, as discussed below.

For steady-state problems, the wetting velocity is equal in magnitude but opposite in sign to the component of the substrate velocity normal to the wetting line, or,

$$u_{wet} = -\boldsymbol{n}_{cl} \bullet \boldsymbol{u}_w \tag{2}$$

that is, the fluid wets outward as fast as the substrate carries it in. It is this condition which permits a smooth transition along the wetting line from dynamic behavior to static behavior where

the substrate moves parallel to the wetting line and the wetting velocity is zero. When (2) is substituted into (1), it is found that the fluid velocity at the contact line, $\boldsymbol{u}$, does not have a component normal to the contact line:

$$\boldsymbol{n}_{cl} \bullet \boldsymbol{u} = 0 \tag{3}$$

We call this the *edge kinematic* condition for steady-state problems. Recall that $\boldsymbol{n}_{cl}$ is a unit vector normal to the wetting line in the plane of the substrate.

An additional assumption is that the fluid slips only normal to the contact line and does not slip tangentially. Yet more precisely, the physics of wetting at the wetting line do not induce tangential velocity in the fluid which is different from the tangential velocity of the substrate. Thus,

$$\boldsymbol{t}_{cl} \bullet \boldsymbol{u} = \boldsymbol{t}_{cl} \bullet \boldsymbol{u}_w \tag{4}$$

By this equation, the fluid velocity tangent to the contact line varies with the contact line orientation and once again permits smooth transition from a dynamic wetting line to a static wetting line where the fluid at the wetting line moves with the same velocity as the substrate.

Finally, in most problems of interest the fluid does not penetrate into the substrate:

$$\boldsymbol{n}_w \bullet \boldsymbol{u} = 0 \tag{5}$$

Equations (3), (4), and (5) constitute three constraints on the velocity which replace the fluid momentum equation along the contact line in steady-state problems and allow us to resolve the paradox. However, they apply only when the contact line is not moving in time. In transient problems, the model of the wetting velocity must now include the normal component of the mesh velocity at the contact line, $\dot{\boldsymbol{x}}_{fs}$

$$u_{wet} = -\boldsymbol{n}_{cl} \bullet \boldsymbol{u}_w + \boldsymbol{n}_{cl} \bullet \dot{\boldsymbol{x}}_{fs}, \tag{6}$$

and equations (3), (4), and (5) generalize as follows:

$$\boldsymbol{n}_{cl} \bullet (\boldsymbol{u} - \dot{\boldsymbol{x}}_{fs}) = 0; \boldsymbol{t}_{cl} \bullet \boldsymbol{u} = \boldsymbol{t}_{cl} \bullet \boldsymbol{u}_w; \text{ and } \boldsymbol{n}_w \bullet (\boldsymbol{u} - \dot{\boldsymbol{x}}_{fs}) = 0. \tag{7}$$

The tangential motion of the mesh at the contact line has no physical meaning and so is left out of the tangential constraint on the fluid velocity. It is clear that the transient relations reduce to the steady state relations when $\dot{x}_{fs} = 0$.

Variable Contact Angles for 3D Dynamic Contact Lines

To illustrate and test the requirements for a three dimensional contact line model, we consider a droplet of fluid descending an inclined plane at a constant velocity. At the leading edge of the droplet, the contact line is *advancing* with respect to the substrate at a constant velocity. At the trailing edge the contact line is *receding* at the same constant velocity. At all other points, the contact line advances or recedes normal to itself at velocities that are some fraction of the overall speed of descent. There are at least two points where it neither advances nor recedes (in the normal direction). Assuming a constant wetting speed around the edge of the droplet would result in an unrealistic prediction of a droplet that spreads without bound.

Furthermore, there is a wealth of experimental evidence that indicates, for a given fluid in contact with a given substrate, that the dynamic contact angle is most dependent upon its rate of advance or recession (see Blake and Ruschak[18]). This rate can be expressed as the normal component of the relative velocity of the free surface at contact line and the substrate,

$$\dot{x}_{wet} = \boldsymbol{n}_{cl} \bullet (\dot{\boldsymbol{x}}_{fs} - \boldsymbol{u}_w). \tag{8}$$

Therefore, all things being equal, the contact angle at any point on the contact line is a function of $\dot{x}_{wet}$ and the hydrodynamic properties of the fluid:

$$\theta = f(\dot{x}_{wet}, Ca) \tag{9}$$

θ is the dynamic contact angle as illustrated in Figure 2 and $Ca = \mu V/\sigma$ is the capillary number based on a reference velocity V. Thus, the contact angle varies along the contact line. This fact can be easily observed by studying the motion of a raindrop down a windshield and has been suggested previously by others[15,13]. It is perhaps noteworthy that (8) is nearly identical to (6) suggesting an alternative statement of the wetting line model would be $u_{wet} = \dot{x}_{wet}$.

We define a local capillary number, Ca_L which varies along the wetting line.

$$Ca_L = Ca\frac{\dot{x}_{wet}}{V} = Ca\ \ \boldsymbol{n}_{cl} \bullet \left(\frac{\dot{\boldsymbol{x}}_{fs} - \boldsymbol{u}_w}{V}\right) \tag{10}$$

With this definition, an advancing wetting line corresponds to $Ca_L > 0$ while a receding line corresponds to $Ca_L < 0$. Reports in the literature propose many different relationships between dynamic contact angle and wetting speed; they are normally expressed in terms of the capillary number. The results are typically for two-dimensional flow systems so there is usually only a single capillary number associated with the entire contact line. In addition the results often only apply to advancing or receeding contact lines or apply only over a limited range of capillary numbers, e.g. [19,20,21]. To ensure computational robustness a relation is needed that is applicable simultaneously to advancing and receding contact lines and is valid over a large range of capillary numbers. Such a correlation was not immediately available in the literature. Indeed there is evidence that measured dynamic contact angles are also dependent upon the flow geometry itself [22]. Thus, a correlation developed for contact angles from a plunging tape device, for example, might not be appropriate for other problems.

Instead, we used an admittedly simplistic but computationally tractable linear model, as suggested by Kistler[23]:

$$n_w \bullet n_{fs} = \cos\theta = \cos\theta_s - c_T Ca_L = \cos\theta_s - c_T Ca\frac{\dot{x}_{wet}}{V} \tag{11}$$

θ is the contact angle, θ_s is the static contact angle (when $\dot{x}_{wet} = 0$), and c_T is a proportionality constant. The vectors n_w and n_{fs} and the contact angle are depicted in Figure 2 for a two-dimensional contact line. Note that (11) can also be used to set a fixed contact angle by setting $c_T = 0$.

Equation (11) is strictly applicable only for $|Ca_L| \ll 1$. It is also hampered because it can predict contact angles that are greater than $180°$ or less than $0°$. Furthermore, this model does not account for certain well-known phenomena like contact angle hysteresis or critical contact angles. However, the primary goal of this current work was development of an effective and efficient method for solution of problems with three dimensional dynamic contact lines. The linear model provides the essential features of varying contact angles and wetting speeds while being easy to implement computationally. In the future the linear model could be generalized.

Finite Element Formulation

Part I[1] of this two-paper series provides details of the governing partial differential equations and corresponding finite element formulation. The description is extended here to include the application of boundary conditions specific to dynamic wetting lines. The Navier-Stokes equations for an incompressible Newtonian fluid govern the flow within the liquid:

$$Re\left(\frac{\partial \boldsymbol{u}}{\partial t} + \boldsymbol{u} \bullet \nabla \boldsymbol{u}\right) = \nabla \bullet \boldsymbol{T} + St\boldsymbol{f} \tag{12}$$

$$\nabla \bullet \boldsymbol{u} = 0, \tag{13}$$

$\boldsymbol{u}$ is the fluid velocity, $\boldsymbol{T}$ is the total fluid stress tensor, $\boldsymbol{f}$ is a unit vector in the direction of gravity, $Re = \frac{\rho L U}{\mu}$ is the Reynolds number, and $St = \frac{\rho g L^2}{\mu U}$ is the Stokes number.

The finite element mesh conforms to the shape of the fluid domain by a pseudo-solid mesh motion technique discussed elsewhere[1,24]. The mesh on the interior of the domain deforms as though it were a solid according to a quasi-static elastic momentum equation:

$$\nabla \bullet \boldsymbol{S} = 0 \tag{14}$$

$\boldsymbol{S}$ is the stress in the pseudo-solid and is related to the mesh displacement field $\boldsymbol{d}$ by a large-strain Neo-Hookean consitutive equation. The displacement field is determined simultaneously with the velocity and pressure fields.

In addition to these volumetric equations, there are boundary conditions applied at and around the dynamic wetting line. The free surface is constrained by the requirement that it be a material surface, also known as the kinematic requirement,

$$\boldsymbol{n} \bullet (\boldsymbol{u} - \dot{\boldsymbol{x}}_{fs}) = 0 \tag{15}$$

In addition, surface tension forces are present at the free surfaces via

$$\boldsymbol{n} \bullet \boldsymbol{T} = \boldsymbol{n} p_{ext} + 2H\sigma\boldsymbol{n} + \nabla_s \sigma \tag{16}$$

where σ is the surface tension, H the mean surface curvature, and ∇_s is the projection of the gradient operator into the surface, see Part I[1] for additional details. On the solid substrate in a small region adjacent to the wetting line, Navier's slip condition is applied:

$$\boldsymbol{n}_w \bullet \boldsymbol{T} \bullet \boldsymbol{t} = \frac{1}{\gamma}(\boldsymbol{u} - \boldsymbol{u}_w) \bullet \boldsymbol{t} \tag{17}$$

where γ is the Navier slip coefficient and $\boldsymbol{t}$ is a tangent vector in the substrate surface.

In the finite element formulation, approximation fields $\boldsymbol{u}_h$, p_h, and $\boldsymbol{d}_h$ are defined in terms of basis functions, ϕ_i and ψ_i, which are piecewise continuous over every element in the mesh,

$$\boldsymbol{u}_h = \sum_i^{N_u} \boldsymbol{u}_i \phi_i,\ p_h = \sum_i^{N_p} p_i \psi_i, \text{ and } \boldsymbol{d}_h = \sum_i^{N_d} \boldsymbol{d}_i \phi_i \tag{18}$$

The coefficients, $\boldsymbol{u}_i$, p_i, and $\boldsymbol{d}_i$, in these approximations are found by satisfying Galerkin weighted residual equations corresponding to equations (12), (13), and (14) over the whole flow domain:

$$R_i^{m,\beta} = \int_V \phi_i \mathbf{e}_\beta \bullet \left(Re \frac{\partial \boldsymbol{u}_h}{\partial t} + Re(\boldsymbol{u}_h - \boldsymbol{u}_m) \bullet \nabla \boldsymbol{u}_h - Stf \right) dV + \int_V \nabla(\phi_i \mathbf{e}_\beta) : \boldsymbol{T} dV \tag{19}$$

$$- \int_A (\phi_i \mathbf{e}_\beta \mathbf{n} : \boldsymbol{T}) dA = 0$$

$$R_i^c = \int_V \psi_i (\nabla \bullet \boldsymbol{u}_h) dV = 0 \tag{20}$$

$$R_i^{d,\beta} = \int_V \nabla(\phi_i \mathbf{e}_\beta) : \boldsymbol{S} dV - \int_A (\phi_i \mathbf{e}_\beta \mathbf{n} : \boldsymbol{S}) dA = 0 \tag{21}$$

This is the so-called weak formulation of the Navier-Stokes equations because the stress term has been integrated by parts. The stress term in the pseudo-solid momentum equation has likewise been integrated by parts. The continuity equation is converted into a least-squares formulation prior to being solved numerically, as explained in Part I[1].

These equations are solved using a finite element computer program developed at Sandia National Laboratories[25]. In this program the integrals in equations (19) to (21) are evaluated numerically by Gaussian quadrature, and all the residual equations are solved simultaneously by Newton's method.

Part I[1] of this series covered the method for applying boundary conditions on free and solid surfaces. Here we focus on the formulation related to the dynamic contact line. A dynamic contact line is the intersection between a free surface boundary and a solid substrate boundary. Along the free surface boundary, the capillary stress balance is applied to the fluid momentum equations by substitution of (16) into the last term of (19):

$$\int_A \phi_i e_\beta \boldsymbol{n}:\boldsymbol{T}_{in} dA = \int_A \phi_i (e_\beta \bullet \boldsymbol{n}) p_{ext} dA - \int_A \frac{1}{Ca}(\boldsymbol{I} - \boldsymbol{nn}):\nabla(e_\beta \phi_i) dA + \int_S \phi_i \frac{1}{Ca}(e_\beta \bullet \boldsymbol{m}) dS \qquad (22)$$

Also along the free surface boundary, the strong integrated (penalized) form of the kinematic condition is applied in place of the pseudo-solid mesh motion equations:

$$R_i^{d,n} = \int_A \phi_i \boldsymbol{n} \bullet (\boldsymbol{u} - \dot{\boldsymbol{x}}_{fs}) dA \qquad (23)$$

This equation insures that there is no flux of fluid across the free surface. The superscript n indicates that this equation replaces the normal component of the mesh displacement equation for node i. As discussed in Part I[1], the pseudo-solid mesh motion equations are rotated into normal and tangential form along the free surface; the kinematic condition replaces the normal component.

Over the portion of the solid substrate in contact with the liquid, except for a thin region near the dynamic contact line, we assume no slip between the substrate and the fluid. The no slip conditions are applied as Dirichlet conditions on the Navier-Stokes residual equations, (19). In a thin region of the solid substrate boundary near the dynamic contact line, we allow tangential slip using the Navier Slip condition, applied by substituting equation (17) into the boundary term of (19):

$$\int_A \phi_i e_\beta \boldsymbol{n}:\boldsymbol{T}_{in} dA = \int_A \phi_i \frac{1}{\gamma} e_\beta \bullet (\boldsymbol{u} - \boldsymbol{u}_w) dA \qquad (24)$$

The normal component of (24) is never used because the impenetrability constraint, (5), replaces the normal component of the momentum equation that contains it.

A planar shape of the solid substrate boundary is imposed by a plane condition as discussed in Part I[1]:

$$R_i^{d,n} = ax_i + by_i + cz_i + d \tag{25}$$

Along the dynamic contact line, three boundary conditions are needed on both the fluid momentum equation and the pseudo-solid mesh motion equation. Equations (7) replace the three components of the momentum equation on the dynamic contact line. These equations represent no penetration into the substrate, no slip tangential to the contact line and the edge kinematic condition. Because all three components of the momentum equation are replaced by boundary conditions, rotation of the momentum equation at the contact line is not necessary. The impenetrability condition is applied as a Dirichlet condition; i.e. the velocity component normal to the substrate is explicitly set to zero. The no-tangential-slip condition and edge kinematic condition are applied as point collocated boundary conditions at gauss integration points along the contact line; i.e. the boundary conditions are evaluated at these discrete points along the contact line of the element edge and used to replace the fluid momentum equations of the nodes on the element edge.

The contact angle condition of equation (11) and the geometric shape of the substrate (as in (25)) constrain the mesh motion along the contact line. To allow the mesh to redistribute tangentially along the contact line, we rotate the components of the pseudo-solid mesh motion equations into components normal to the substrate, tangent to the contact line, and binormal to the contact line (outward pointing normal in plane of substrate):

$$\begin{bmatrix} R_i^n \\ R_i^t \\ R_i^b \end{bmatrix} = \begin{bmatrix} \boldsymbol{n}_{cl,i}^T \\ \boldsymbol{t}_{cl,i}^T \\ \boldsymbol{b}_{cl,i}^T \end{bmatrix} \begin{bmatrix} R_i^x \\ R_i^y \\ R_i^z \end{bmatrix} \tag{26}$$

$\boldsymbol{n}_{cl,i}$ is a vector normal to the substrate surface at node i, $\boldsymbol{t}_{cl,i}$ is a vector tangent to the dynamic contact line, and $\boldsymbol{b}_{cl,i} = \boldsymbol{n}_{cl,i} \times \boldsymbol{t}_{cl,i}$ is a binormal vector which is perpendicular to both $\boldsymbol{n}_{cl}$ and $\boldsymbol{t}_{cl}$ and outward pointing from the wetting line in the substrate surface. Part I[1] discusses the calculation of these nodal unit vectors.

Along the dynamic contact line, the normal component of the rotated pseudo-solid mesh motion equation is replaced by the planar boundary condition (25) as discussed in Part I[1]. The contact angle condition, (11), is applied as a weighted residual equation integrated along the contact line:

$$\int_S \phi_i(\cos\theta - (\cos\theta_s - c_T Ca_L))dS = 0 \tag{27}$$

This weighted residual replaces the binormal component of the pseudo-solid mesh motion equation. The local capillary number is calculated according to equation (10). We retain the remaining tangential component of the rotated psuedo-solid momentum equation to allow the nodes to slide freely along the dynamic contact line. If this step is omitted, spurious sources of mesh stress will be introduced at the contact line.

Results

Capillary Rise in a Corner

When a fluid wets the walls of its container, the meniscus rises near the wall to balance gravitational and capillary forces. Results of the meniscus shape are well tabulated for two-dimensional problems where the free surface is a curve. Brown[26] and others have calculated the shapes of mensici for three-dimensional problems without gravity where the mean curvature is constant. We use capillary rise with gravity as a simple test problem for the contact angle formulation discussed above. Figure 3 shows predictions of the meniscus shape for capillary rise in a box at various contact angles. The container is a box with smooth, vertical walls; the solution is obtained for a quarter of the box by imposing symmetry at the vertical mid-planes. There is no-slip of the fluid on the boxes walls, and at steady state the velocity is zero everywhere within numerical accuracy. The bottom of the box is an open boundary with a specified pressure; this pressure and the external pressure determine the depth of liquid in the box ($\Delta p = \rho g h$).

The top surface of the fluid is the free surface which moves to balance capillary and pressure forces via the capillary condition and to conserve mass via the kinematic condition. The side walls, symmetry planes, and bottom boundary restrict the mesh position by geometric plane cond-

tions. The free surface intersects the symmetry planes at a right angle and intersects the walls at specified contact angles. In the corner where the walls meet, two contact angle conditions, two geometric planar conditions and the kinematic condition all apply to the mesh equation at the same point. However, only three independent boundary conditions can apply to the pseudo-solid mesh motion equation at any point, so two of the boundary conditions need to be eliminated there. We tested several choices of boundary conditions at this corner and determined that the most effective method is to apply both the geometric planar constraints and the kinematic condition. Nevertheless, the contact angle conditions are still well satisfied up to the corner.

The predictions in Figure 3 show that the meniscus rises near the walls due to fluid wetting but becomes nearly flat at the center of the box. The meniscus rises highest in the corner due to additional curvature from bending the rising mensicus around the corner; i.e. near the corner the second radius of curvature contributes significantly to the pressure drop across the interface. Far from the corner, the second radius of curvature is nearly infinite and the meniscus shape approaches that of a translationally symmetric interface. As the contact angle decreases (fluid wets solid better), the fluid wicks higher onto the walls and into the corner.

The contact angles on the two walls do not have to be equal. Figure 3 shows the capillary rise near a corner between two walls with contact angles 60 and 120. In this case, fluid rises on the wall with a contact angle of $60°$ and descends on the wall with contact angle of $120°$. In the corner where the walls meet, the meniscus height is equal to the height of the meniscus at the center of the box. This is a simple example demonstrating the application of our contact angle formulation to three-dimensional free surface problems. In the next two sections we apply the formulation to problems with fluid flow.

Initial motion of droplet down an inclined plane

The motion of a droplet down an inclined plane is a problem that, despite its prosaicness, has not received much attention. Dussan and Chow[15] developed perturbation solutions valid for small capillary numbers, contact angles, and inclinations to the critical configuration for motion and the configuration for steady state motion. Later, Dussan[16] extended this work for arbitrary

contact angles. Dimitrakopoulos and Higdon[13] used boundary element methods to also compute the criticial configuration prior to motion.

The contact line conditions discussed previously have been applied to the motion of an initially quiescent droplet down an inclined plane. Figure 4 shows the initial droplet shape and the finite element mesh employed in the solution. This configuration was obtained from an originally hemispherical shape. A gravitational acceleration was applied along the z axis and the droplet was allowed to deform over time to the final shape shown in Figure 4. The computational domain used was actually only half of the region shown in Figure 4 since the x = 0 plane was taken as a symmetry plane. This had the benefit of reducing the number of unknowns for this lengthy transient calculation and also provided determinacy to the mesh displacement unknowns. Without this step, unphysical rotary modes of mesh motion about the z axis could appear in the phase of the calculation when there was no inclination.

The free surface of the droplet is subject to the kinematic constraint, (23). No slip was enforced on the underside of the droplet, except in a narrow annular band of elements adjacent to the contact line. On these elements the Navier slip condition, (24), was employed. Its purpose was to permit transition from the no-slip condition in the interior to the contact line velocity conditions described in a earlier section. The slip coefficient, γ, was taken as 0.01.

During the computation it became necessary to "anneal" the mesh. It was observed that as the droplet moved further and further from its starting point, the larger and larger displacements would begin to inhibit convergence of the iterative solver. It was therefore necessary periodically to update the coordinates of each node with its respective displacement vector and restart the problem with a zero displacement field, effectively removing the mesh stresses. The velocity and pressure fields, however, were not changed. This is a viable procedure because ultimately it is the position of the mesh nodes and not their displacement from a reference state that interacts with the other unknown fields.

On the contact line, the momentum equations were replaced by the three conditions given by (7). Since the substrate is motionless for this transient problem, the web speed, u_w, was set to

zero. The linear relationship between contact angle and local capillary number, (11), was used to determine the local contact angle. For this example calculation, *ad hoc* values for the parameters in this model were chosen. The static contact angle, θ_s, was set at 90 and the linear constant, c_T at 0.99. The latter value is somewhat meaningless but for the fluid modeled it would result in a 180° contact angle at a droplet speed of 720 cm/s. Thus, the contact line is fairly slippery.

The fluid modeled had physical properties similar to water: $\rho = 1$ g/cm^3, $\mu = 0.1$ dyn s/cm^2, and $\sigma = 72$ dyn/cm. The viscosity is roughly ten times that of water at room temperature and this value was chosen to mitigate inertial effects on the mesh distortion in the initial computation from the hemisphere to the stable deformed shape.

At time zero, a gravitational acceleration vector is rotated 30° towards the x axis, that is, the substrate is tipped 30 degrees downward in the x direction. The subsequent motion is depicted in Figure 5, which shows side and planform views of the droplet at several times. Note the size of the grid scale. Overall fluid tends to shift to its downhill side and the droplet becomes elongated longitudinally. Ultimately, a "rooster tail" appears in the free surface at the trailing edge. This more than likely is the result of the distortion in the mesh in this region. A remeshing of the domain would be required to continue. This was not done.

Laydown of a Bead on a Moving Substrate

Another problem that includes a three dimensional dynamic contact line is the extrusion of a liquid onto a moving substrate. We refer to this as the 'bead laydown' problem. Examples of this type of process can be found in fields as diverse as free-casting of complex parts to food processing. It is a challenging problem because the contact angle on the horseshoe shaped contact line changes continually from a maximum value at the leading edge, where the motion of the substrate is perpendicular to the line, to a static value downstream of the nozzle, where the motion of the substrate is parallel to the contact line and the fluid moves as a rigid body along with the substrate.

Figure 6 depicts the geometry and the starting shape of the finite element mesh. The proportions shown are based upon an actual experimental apparatus with a $D = 0.127$ cm nozzle diame-

ter. The nozzle lies 0.89D above the substrate and the horizontal portion of the mesh extends approximately 5D downstream of the nozzle. The y = 0 plane is a symmetry plane, and this was exploited to reduce the number of unknowns by solving only one-half of the problem. The mesh shown in Figure 6 contains 2691 elements, 3296 nodal points and 23072 unknown degrees of freedom.

The boundary conditions applied to this mesh are depicted in Figure 7. No slip is applied on the walls of the nozzle. The kinematic condition, (23), is enforced on the free surface as shown; the free surface deforms to satisfy this constraint. On the symmetry plane, zero normal velocity is enforced; otherwise, the fluid is allowed to slip tangentially on this boundary. On the underside of the mesh, where the fluid adheres to the moving substrate, no slip between substrate and fluid is enforced except along a narrow band of elements adjacent to the contact line. As in the case of the droplet problem, a Navier slip condition is applied in this region. The conditions applied along the contact line to the momentum and pseudo-solid mesh equations are the same as those applied in the droplet problem but changed for steady state conditions.

A study examining the effect of several input parameters was conducted. The fluid modeled was based upon a silicon oil standard fluid with density of 1 g/cm^3 and viscosity 1024 P. These properties were fixed, but the surface tension was varied to obtain different values of the global capillary number. The surface tension values considered were in general much larger than the actual fluid's for reasons which will be discussed below. Contact angle data were not available. Instead, the parameters of the contact angle model were varied in order to study the effects of the contact angle model. However, the parameters were not varied independently. For a given static contact angle, the slope parameter, c_T, was adjusted so the contact angle at the leading edge of the bead would always be 175°. This was done to reflect the experimental observation for this highly viscous fluid that the contact angle at the leading edge was generally very close to 180°.

The results of this parameter study are shown in figures 8 through 10. Each figure gives three different views of the free surface shape: from left to right, front, side and underside or web-side. The underside views are presented in a split view format; one half the domain is shown in

"hidden view" format, but the other half is shown in "wireframe" format. This allows for locating the contact line with respect to the inlet nozzle.

Figure 8 shows the effect of changing the ratio of the average inlet liquid velocity to substrate speed on the steady free surface shape. The static contact angle was fixed at 110°. The capillary number based upon the speed of the web was 1.0. The ratio of average inlet liquid velocity to web speed presented are, from top to bottom, 1.0, 1.6. 2.5, and 3.2, respectively. The behavior is generally what one expects. As the inlet flow is increased with a fixed web speed, the fluid tends to pile up around the nozzle, billowing to the sides and ahead of the nozzle. At the highest ratio, the contact line has advanced almost one-half a diameter ahead of the nozzle. In addition, the contact line contracts back towards the symmetry plane at a distance downstream from the nozzle. This is accompanied by the ridgeline of the bead rising to a height that is greater than the gap between nozzle and substrate. This behavior is a consequence of the relatively high surface tension present, which tends to contract the bead from its splayed out configuration in the vicinity of the nozzle to a more hemispherical configuration downstream where the influence of the nozzle has disappeared.

Figure 9 shows the influence of surface tension on the free surface shape. At a speed ratio of 1.6, the figure depicts the response at capillary numbers of 0.5, 1.0 and 2.0. Again the static contact angle was fixed at 110°. Although the changes in the free surface shape are smaller than the previous case, it is clear and expected that the liquid tends to spread out more as the capillary number increases, i.e. as an effect of the diminished surface tension. It is worth noting that convergent results were not obtained for Ca greater than approximately 2.0. Surface tension has the effect of stabilizing the free surface; as it is decreased, oscillations tend to appear in the free surface. This was especially true for the mesh used in this study. Because of the large distortion on the free surface, the elements at the leading edge near the contact line had become large in the dimensions parallel to the web but very narrow in the direction perpendicular to it. Oscillations were observed on a portion of the free surface including these elements. This is the reason that the actual surface tension of the silicon oil could not be used; its high viscosity resulted in too large a capillary number. Although not undertaken here, this problem may be alleviated by better refinement of the area nearest the contact line.

Finally, Figure 10 shows the influence of the static contact angle. Here, the slope of the contact angle model was not set to ensure a specific contact angle at the leading edge, but instead held constant. The ratio of inlet average liquid velocity to web was again 1.6 and the surface tension of the fluid was set to give a global capillary number of 1.0. The views shown in this figure are for static contact angles of 110°, 80°, 60°, and 45°, top to bottom. The front view clearly shows the strong influence of this parameter at the downstream outlet where the normal contact line velocity is smallest. Near the nozzle its influence is less, although still noticeable. The results are also in agreement with our expectations: the liquid spreads out to a greater extent for the lower static angles, which imply a greater propensity for wetting. The influence of the slope parameter, c_T, was also conducted, however, it was found that it did not have a tremendous effect on the overall shape of the free surface.

Comparison with Experiments

We have made some preliminary steps towards direct comparison of these simulations with experiment. A second standard silicon oil was chosen for visualization. Its viscosity is 126.4 P. Its density was found to be 1 g/cm^3 and a value of 20 dyne/cm for surface tension was obtained from the literature as a typical value[27]. Because of its (relatively) low viscosity, consistency could be achieved between experimental global capillary numbers and those accessible to numerical computations (unlike the previous set of comptuations). By extruding this fluid onto a moving glass platform, records could be made of the shape of the free surface and the shape and location of the dynamic contact line over a range of flow rates and table speeds. Figure 11 shows the results at one flow rate and table speed. The outline of the free surface and the contact line has been highlighted in white in the photographs. The average inlet velocity was 0.64 cm/s and the web speed was 0.2 cm/s, that is, the ratio of inlet liquid flowrate to web speed was 3.2. The inside nozzle diameter in this case was 0.137 cm. The capillary number computed from the speed of the web was 1.3. A 90° static contact angle was used in the simulation. This value was chosen because, lacking any additional data, it would have the smallest potential error, namely 90°, of any other value. The value for c_T was obtained from the static contact angle as explained above.

In general, the qualitative shape of the computed contact line is similar to the experimental observation in that both are smoothly-varying and parabola shaped. However, the calculated contact line lies well in advance of the nozzle exit. In contrast, the experimental contact line is almost directly below the upstream side of the nozzle exit. Further the lateral spread of the computed contact line extends to more than a nozzle diameter away from the centerline plane. The experimental contact line extends outward to a lesser extent. Comparison of bead ridge behind the nozzle cannot be made because the actual fluid has wetted up the backside of the nozzle obscuring this portion of the photo.

That the agreement is less than desirable is attributable to at least two possibilities. First, the distortion of the elements in the vicinity of the contact line leading edge (i.e. the front) has expanded the region where the Navier slip condition is applied to an extent that is probably unreasonable. Figure 12 shows the computed axial velocity of the fluid on the interface between fluid and moving web. Over most of the region this component is uniformly the web speed, as it should be, but over a significant region near the leading edge of the bead, it differs significantly from the web speed. This could have the effect of allowing the contact line to advance ahead of the nozzle contrary to the experimental evidence. Second as noted above, the contact angle model is probably too simplistic. While it captures the gross features needed in a contact angle model, it probably fails to predict detailed dependencies on the wetting parameters. A more realistic behavior is depicted in Figure 13 where the contact angle changes rapidly for values of capillary number nearest to zero, but approaches contant values as the local capillary number becomes larger. Finally, we note that the parameters in the contact angle model were not based in any quantitative way on actual observations, but chosen for the most part arbitrarily Given these limitations it is not surprising that agreement is lacking.

Discussion

This work extends the body-fitted three dimensional free surface method described in Part I[1] to include problems that possess three dimensional static and dynamic wetting lines. Static wetting lines are described by a single static contact angle along each wetting line. Dynamic wetting lines are more complicated for several reasons. The kinematic paradox needs to be circumvented

appropriately in three dimensions. Our approach is to assume that the fluid velocity at the wetting line and the wetting line velocity itself have the same normal component with respect to the substrate. The tangential component of the fluid velocity remains unaffected and is equivalent to the tangential component of the substrate velocity. Furthermore, for most practical problems in three dimensions, the dynamic contact angle must vary along a three dimensional wetting line simply because the motion of the wetting line with respect to the substrate also changes. A model of the contact angle must allow a range of contact angles based upon the local rate of advancement or recession.

These modifications of the standard two-dimensional dynamic contact line formulation allow successful solution of the problems presented in this paper. The pseudo-solid approach to mesh motion, as explained in Part I[1], has shown considerable promise in three dimensions. Its ability to precisely locate the free surface and the wetting line has been instrumental in being able to apply these specialized and highly localized wetting line boundary conditions.

The sliding droplet computation represents an obvious application of our approach. It was observed that fluid would tend to shift to the downhill side of the droplet as time progressed. Further, the entire droplet became stretched in the flow direction but contracted in the direction transverse to the flow. Combined these effects resulted in the planform profile of the droplet evolving from an initial circular shape into the classic "tear drop" shape. Another contact angle model, in particular one that included critical contact angle behavior, would result in a different shape[15]. We note also that at later times a hump of fluid appeared just in advance of the trailing edge. However, because the mesh there had become considerably distorted, we were unable to conclude that this was a true feature.

The bead laydown results have provided an opportunity to examine the shape of the wetting line to changes in operating and/or physical parameters. In general, the contact line was parabolic in form in the vicinity of the nozzle but evolving into a straight line parallel to the web motion downstream. Changing the flowrate did not alter this basic pattern except that for larger inlet velocities the contact line would become broader and further from the nozzle. We did note an important effect of surface tension on the downstream contact line behavior. For relatively large

values of surface tension, the contact line would contract back towards the centerline plane accompanied by the rise of the free surface ridgeline behind the nozzle. This imparted a "paddle" shape to the overall contact line. As the surface tension decreased, this effect diminished. The static contact angle, however, had the most dramatic effect on the contact line shape. The smaller this parameter the further the contact line would spread downstream of the nozzle. Its effect was less pronounced in the region near the nozzle where the effects of the nozzle itself still dominate.

A number of issues still remain. The primary focus of this paper was development of an appropriate method for treating three dimensional free surface problems with static and dynamic wetting lines. Having accomplished that, the next step is to address its deficiencies. The lack of stability of the free surface at higher capillary numbers is probably a result of inappropriately shaped elements. However, this premise needs to verified on a better mesh. The lack of agreement with respect to the experimental visualization results is unfortunate but not unexpected given the focus on development of a numerical method. Better meshes and more appropriate contact angle models should improve agreement.

Nonetheless, the impact of these results should not be minimized. Static contact lines in three dimensions have received only a small amount of attention and dynamic contact lines even less. This should be contrasted with the vast amount of literature pertaining to two-dimensional dynamic contact lines. This paper represents a first in computational fluid mechanics in that there are few if any other computational studies of three dimensional dynamic wetting lines. We believe that we have laid the theoretical and computational groundwork for continued exploration and development of this new area of computational science.

Sandia is a multiprogram laboratory operated by Sandia Corporation, a Lockheed Martin Company, for the United States Department of Energy under contract DE-AC04-94AL85000.

References

1. Cairncross, R.A. , P.R. Schunk, T.A. Baer, P.A. Sackinger, R.R. Rao, "A finite element method for free surface flows of incompressible fluid in three dimensions, Part I: Boundary-Fitted mesh motion.", to be published, (1998).

2. Adamson, H.W., *Physical Chemistry of Surfaces*, 4th ed., Wiley, New York, (1982).

3. Dussan V, E.B, "On the spreading of liquids on solid surfaces: static and dynamic contact lines," *Ann. Rev. Fluid Mech.*, **11**, 371, (1979).

4. Kistler, S.F., "The fluid mechanics of curtain coating and other related viscous free surface flows with contact lines," PhD thesis, University of Minnesota, (1984)

5. Christodoulou, K.N., and L.E. Scriven, "The fluid mechanics of slide coating," *J. Fluid Mech.*, **208**, 321, (1989).

6. Christodoulou, K.N., S.F. Kistler, and P.R. Schunk, " Advances in computational methods for free surface flows," in Liquid Film Coating, ed. S.F. Kistler and P.M. Schweizer, Chapman and Hall, London, (1997).

7. Schunk, P.R., and L.E. Scriven, "Surfactant effects in coating processes," in Liquid Film Coating, ed. S.F. Kistler and P.M. Schweizer, Chapman and Hall, London, (1997).

8. Christodoulou, K.N., and L.E. Scriven, "Singular elements at dynamic wetting lines," unpublished, (1990).

9. Lowndes, J., "The numerical simulation of the steady movement of a fluid meniscus in a capillary tube," *J. Fluid Mech.*, **101**, 631, (1980).

10. Zhou, M.-Y., and P. Sheng, "Dynamics of immiscible-fluid displacement in a capillary tube," *Phys. Rev. Lett.*, **64**, 882, (1990).

11. Kistler, S.F. and G. Zvan, "Hydrodynamic models of forced wetting in coating flows," paper read at *44th IS&T* conference, St. Paul, MN, May 12-17, (1991).

12. Christodoulou, K.N., and L.E. Scriven, "The physics of slide coating, dynamic wetting, air entrainment," *AICHE Spring National Meeting*,Orlando, FL, March 18-22, (1984).

13. Dimitrakopoulos, P., and J.J.L. Higdon, "On the displacement of three-dimensional fluid droplets from solid surfaces in low-Reynolds-number shear flows," submitted to *J. Fluid. Mech.*, (1998)

14. Extrand, C.W., and Y. Kumagai, "Liquid drops on an inclined plane: the relation between contact angles, drop shape, and retentive force," *J. Coll. Inter. Sci.*, **170**, 515. (1995).

15. Dussan, E.B., and R. Tao-Ping Chow, "On the ability of drops or bubbles to stick to non-horizontal surfaces of solids," *J. Fluid Mech*, **137**, 1, (1983).

16. Dussan V, E.B. "On the ability of drops or bubbles to stick to non-horizontal surfaces of solids. Part 2. Small drops or bubbles having contact angles of arbitrary size," *J. Fluid Mech.*, **151**, 1, (1985).

17. Swartz, L.W. and R.R. Eley "Simulation of droplet motion on low-energy and heterogeneous surfaces." *J. Coll. Inter. Sci.*, **202** (1), 173, (1998).

18. Blake, T.D. and K.J. Ruschak, 'Wetting Static and Dynamic Contact Lines', in Liquid Film Coating, eds. S.F. Kistler and P.M. Schweizer, Chapman and Hall, London, 1997.

19. Jiang, S.F., S.G. Oh, and J.C. Slattery, "Correlation for dynamic contact angle," *J. Colloid Inter. Sci.*, **69**, 74, (1979).

20. Bracke, M., F. De Voeght, and P. Joos, "The kinetics of wetting: the dynamic contact angle," *Progr. Colloid. Polym. Sci.*, **79**, 142, (1989).

21. Chen, K.C., *Studies of Multilayer Slide Coating and Related Processes,* Ph.D. dissertation, Univ. of Minnesota, (1992).

22. Ngan, C.G., and E.B. Dussan V., "On the nature of dynamic contact angle: an experimental study," *J. Fluid Mech.*, **118**, 27, (1982).

23. Kistler, S.F., "Hydrodynamics of Wetting," in *Wettability*, ed. J.C. Berg, M.Dekker, New York, (1993).

24. Sackinger, P.A., P.R. Schunk, R.R. Rao, "A Newton-Raphson Pseudo-Solid Domain Mapping Technique for Free and Moving Boundary Problems: A Finite Element Implementation," *J. Comp. Phys.*, **125**, 83-103, (1996).

25. Schunk, P.R., P.A. Sackinger, R.R. Rao, K.S. Chen, R.A. Cairncross, T.A. Baer, and D.A. Labreche, "GOMA 2.0 - A Full-Newton Finite Element Program for Free and Moving Boundary Problems with Coupled Fluid/Solid Momentum, Energy, Mass, and Chemical Species Transport: User's Guide," SAND97-2404, Sandia National Laboratories, Albuquerque, NM, (1997).

26. Brown, R.A.,"Finite-Element Methods for the Calculation of Capillary Surfaces", *J. Comput. Phys.*, **33**, 217, (1979).

27. *CRC Handbook of Lubrication*, ed. R. Baeger, Boca Raton, FL., CRC Press, 1994.

Figures

Figure 1: Schematic of general three dimensional dynamic wetting line with vector definitions.

Figure 2: Schematic depiction of local contact angle with substrate and free surface normals

Figure 3: Predictions of capillary rise in a box with various values of the contact angle between the free surface and the walls of the box. The pressure distribution is hydrostatic. Contact angles are labelled on each plot.

Figure 4: Mesh and starting configuration of droplet motion calculation. Note that (a) is an oblique view from above of the drop's upper surface. (b) is an oblique view from below of the drops underside. We note that the actual computational domain differs from this figure in that only the domain for which $y \geq 0$ was used as discussed in the text

Figure 5: Planform and side views of initial droplet acceleration down 30° inclined plane at several time points. For scale, the grid appearing in the views is 1 cm on a side. Note the distortion of the mesh at the trailing edge at the last time values.

Figure 6: Mesh and initial undeformed geometry used in bead laydown computation. Since y = 0 is a symmetry plane, only one-half the problem needed to be solved.

Figure 7: Boundary conditions applied to bead laydown domain.

Figure 8: Effect of average inlet fluid velocity to web speed ratio on free surface shape at Ca = 1.0. From top to bottom, ratio values are 1.0, 1.6. 2.5, and 3.2

Figure 9: Effect of surface tension on shape of bead laydown free surface shape. From top to bottom, global capillary numbers are 0.5, 1.0, 2.0. The inlet to web velocity ratio is 1.6.

Figure 10: Effect of static contact angle on shape of bead laydown free surface shape. From top to bottom, static contact angle values are 110°, 80°, 60°, and 45°. The inlet velocity to web velocity ratio is 1.6.

Figure 11: Comparison of experimental visualization of bead laydown free surface shape (top line) and corresponding computed results (bottom line). Ratio of inlet average velocity to web speed: 3.2, global capillary number : 1.3. White line indicates location of free surface and/or dynamic contact line.

Figure 12: Axial velocity component parallel to motion of web on interface plane between fluid and substrate. View is at the underside. Ratio of inlet average velocity to web speed: 3.2, global capillary number : 1.3.

Figure 13: Sketch of features that would be appropriate to a more physically accurate contact angle model.

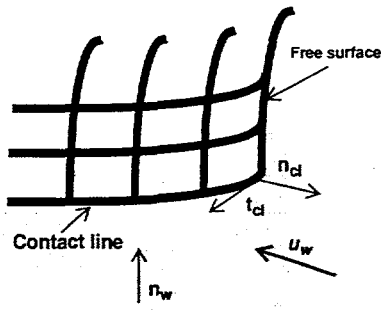

Figure 1 - Schematic of general three dimensional dynamic wetting line with vector definitions.

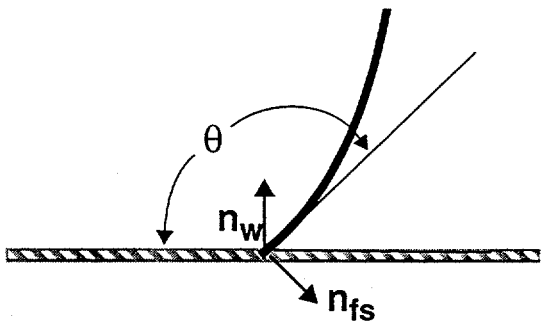

Figure 2 - Schematic depiction of local contact angle with substrate and free surface normals

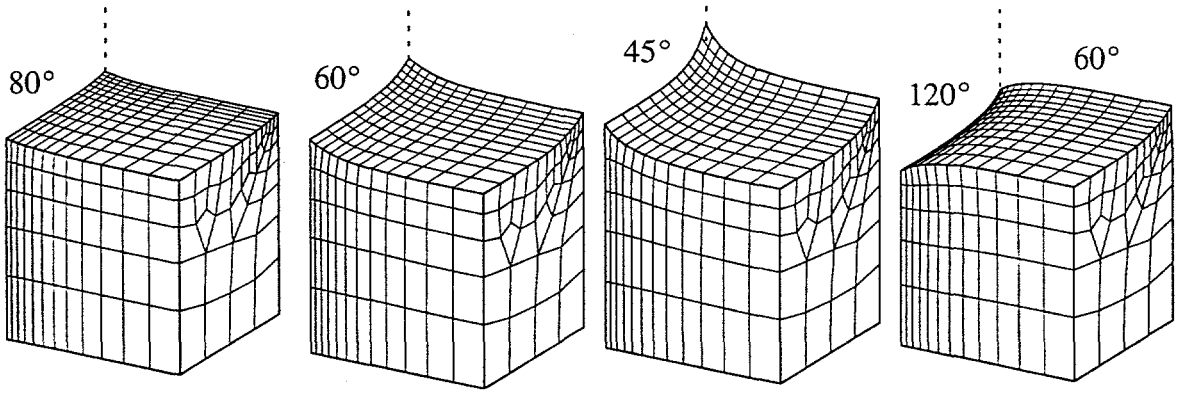

Figure 3 - Predictions of capillary rise in a box with various values of the contact angle between the free surface and the walls of the box. The pressure distribution is hydrostatic. Contact angles are labelled on each plot.

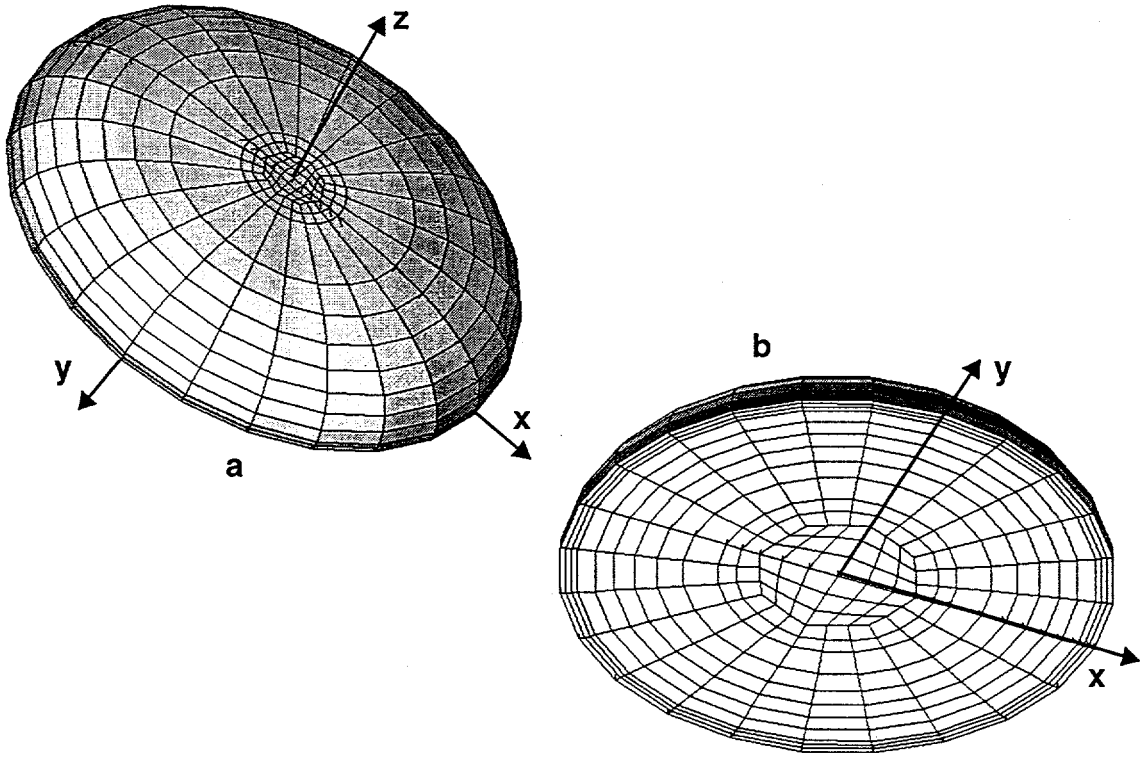

Figure 4 - Mesh and starting configuration of droplet motion calculation. Note that (a) is an oblique view from above of the drop's upper surface. (b) is an oblique view from below of the drops underside. We note that the actual computational domain differs from this figure in that only the domain for which $y \geq 0$ was used as discussed in the text

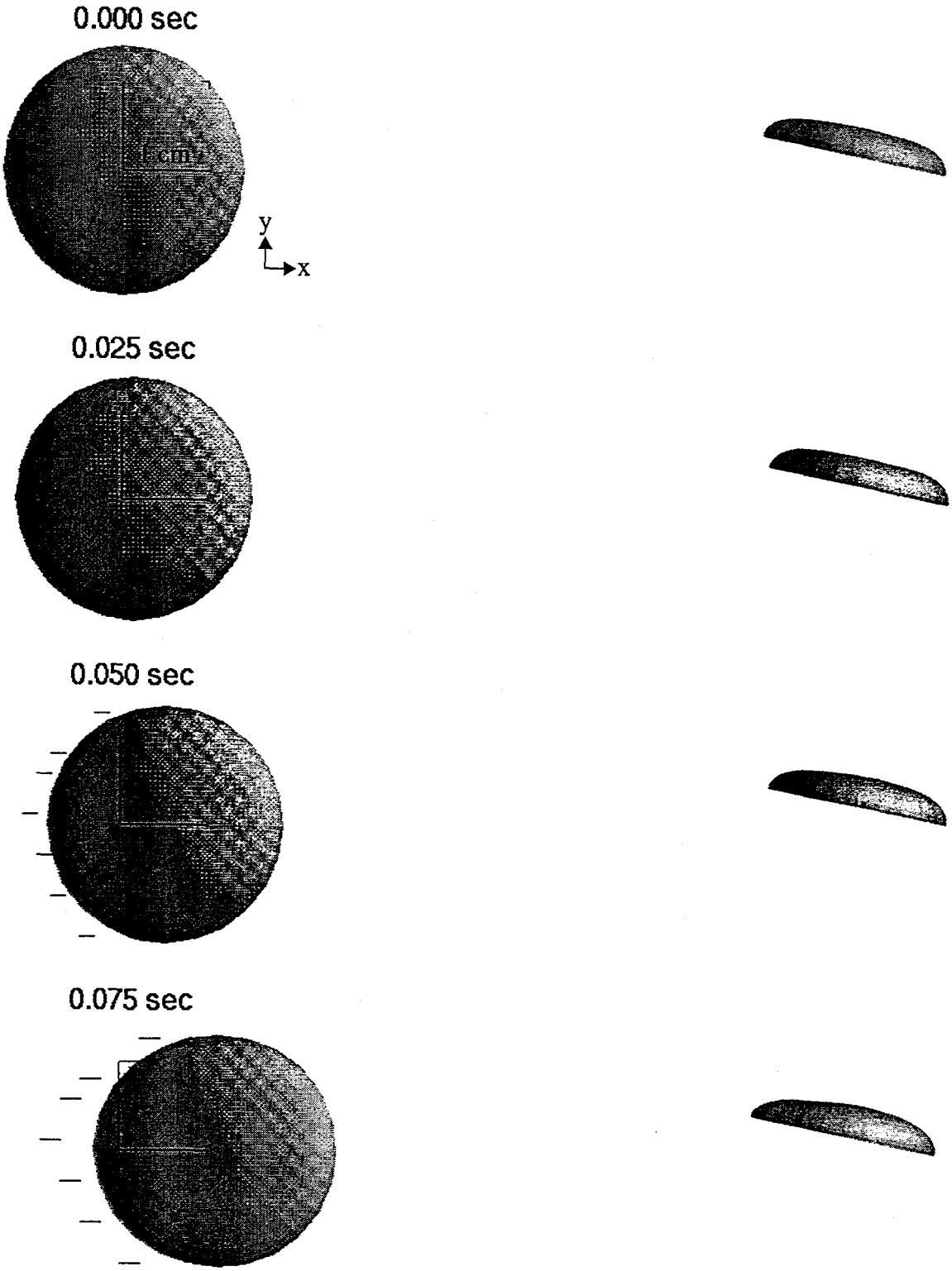
0.000 sec
y
x
0.025 sec
0.050 sec
0.075 sec

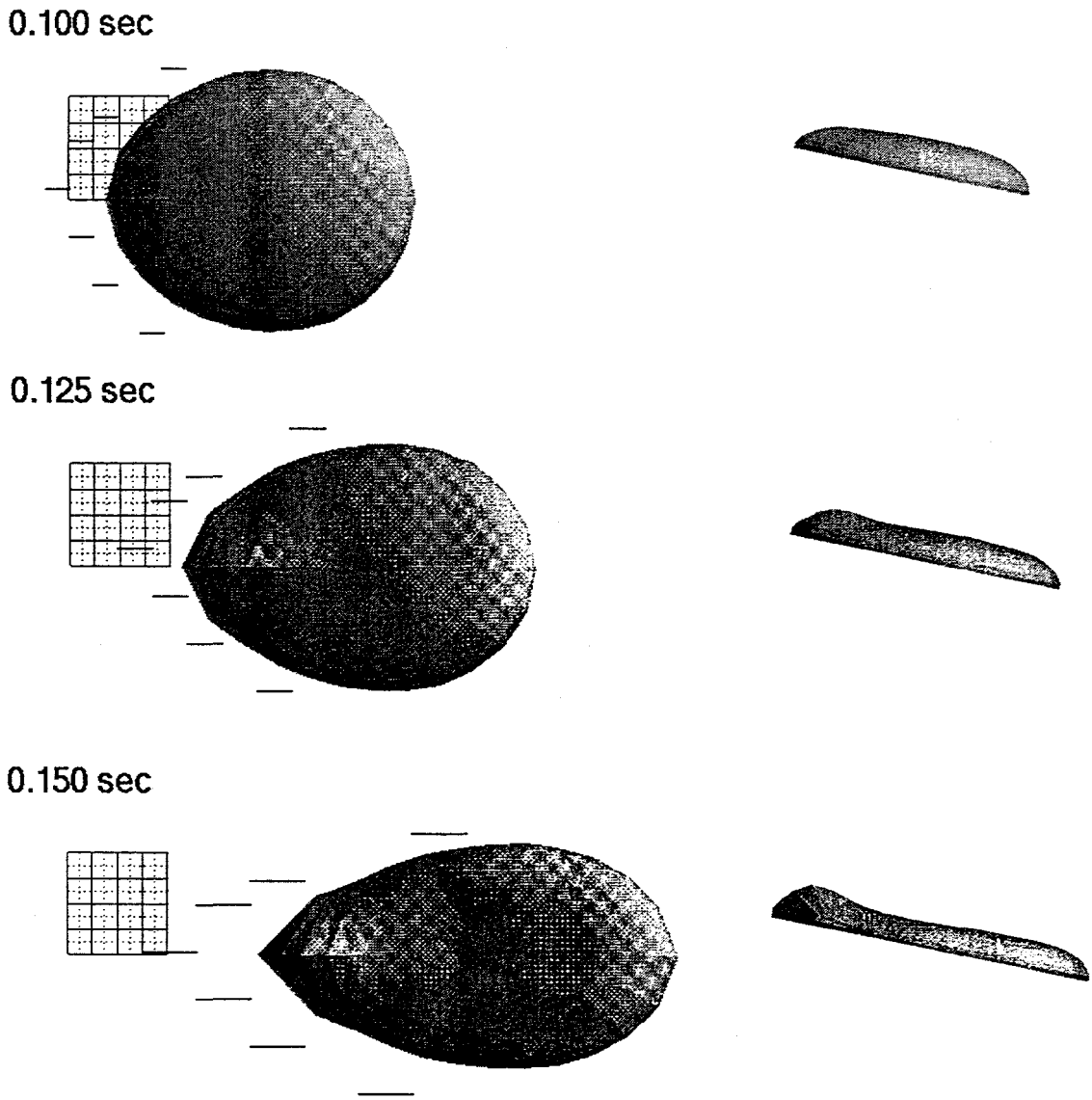

Figure 5 - Planform and side views of initial droplet acceleration down 30° inclined plane at several time points. For scale, the grid appearing in the views is 1 cm on a side. Note the distortion of the mesh at the trailing edge at the last time values.

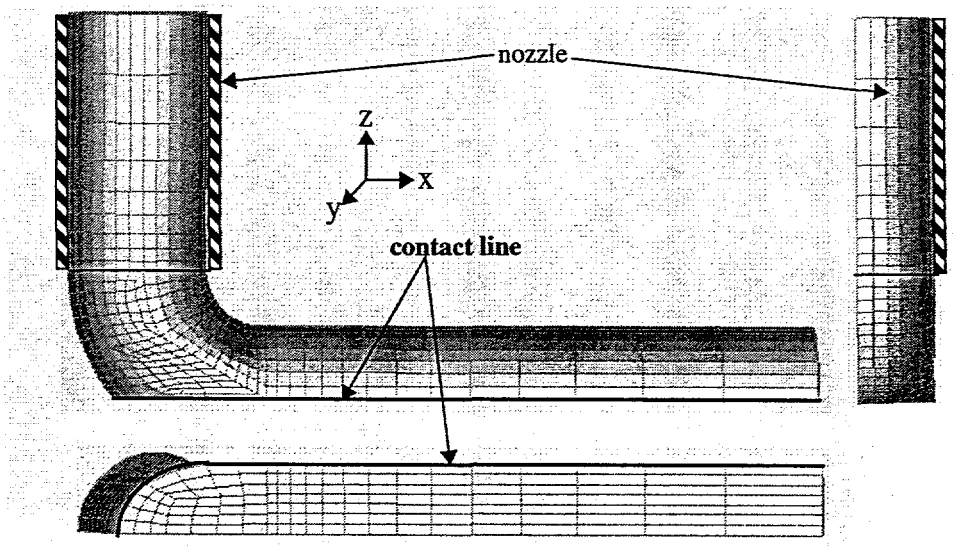

Figure 6 - Mesh and initial undeformed geometry used in bead laydown computation. Since y = 0 is a symmetry plane, only one-half the problem needed to be solved.

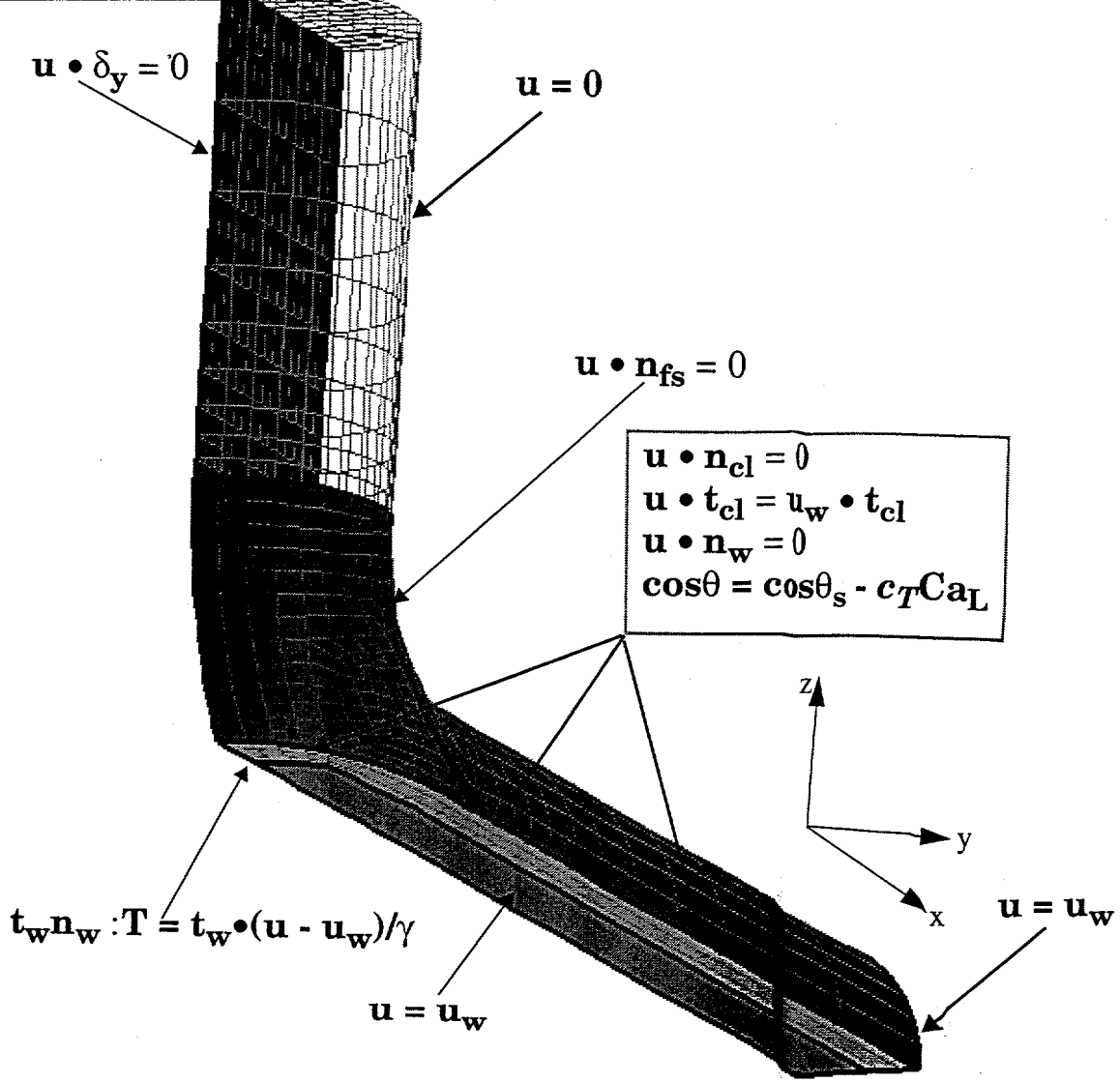

Figure 7 - Boundary conditions applied to bead laydown domain.

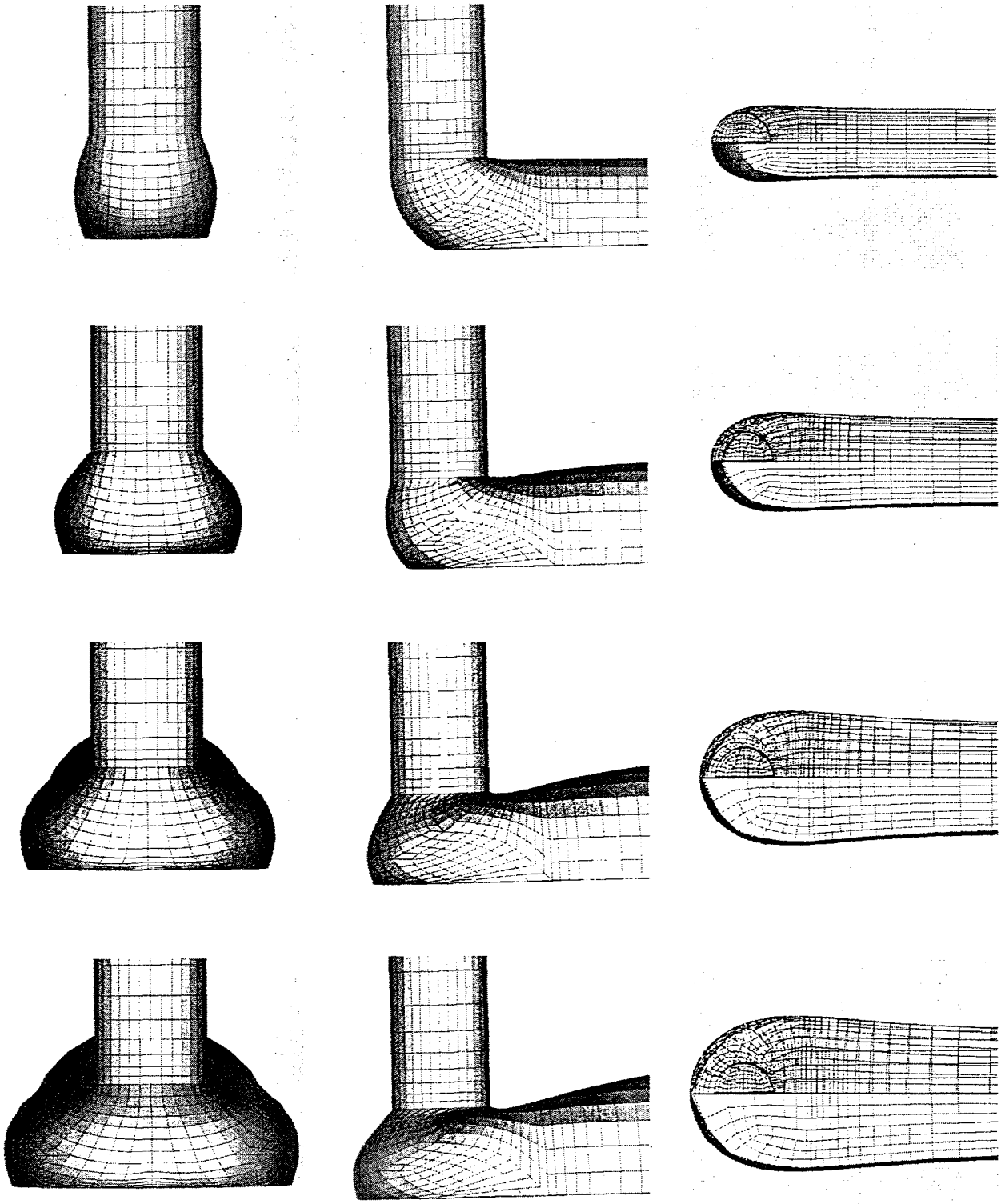

Figure 8 - Effect of average inlet fluid velocity to web speed ratio on free surface shape at Ca = 1.0. From top to bottom, ratio values are 1.0, 1.6. 2.5, and 3.2

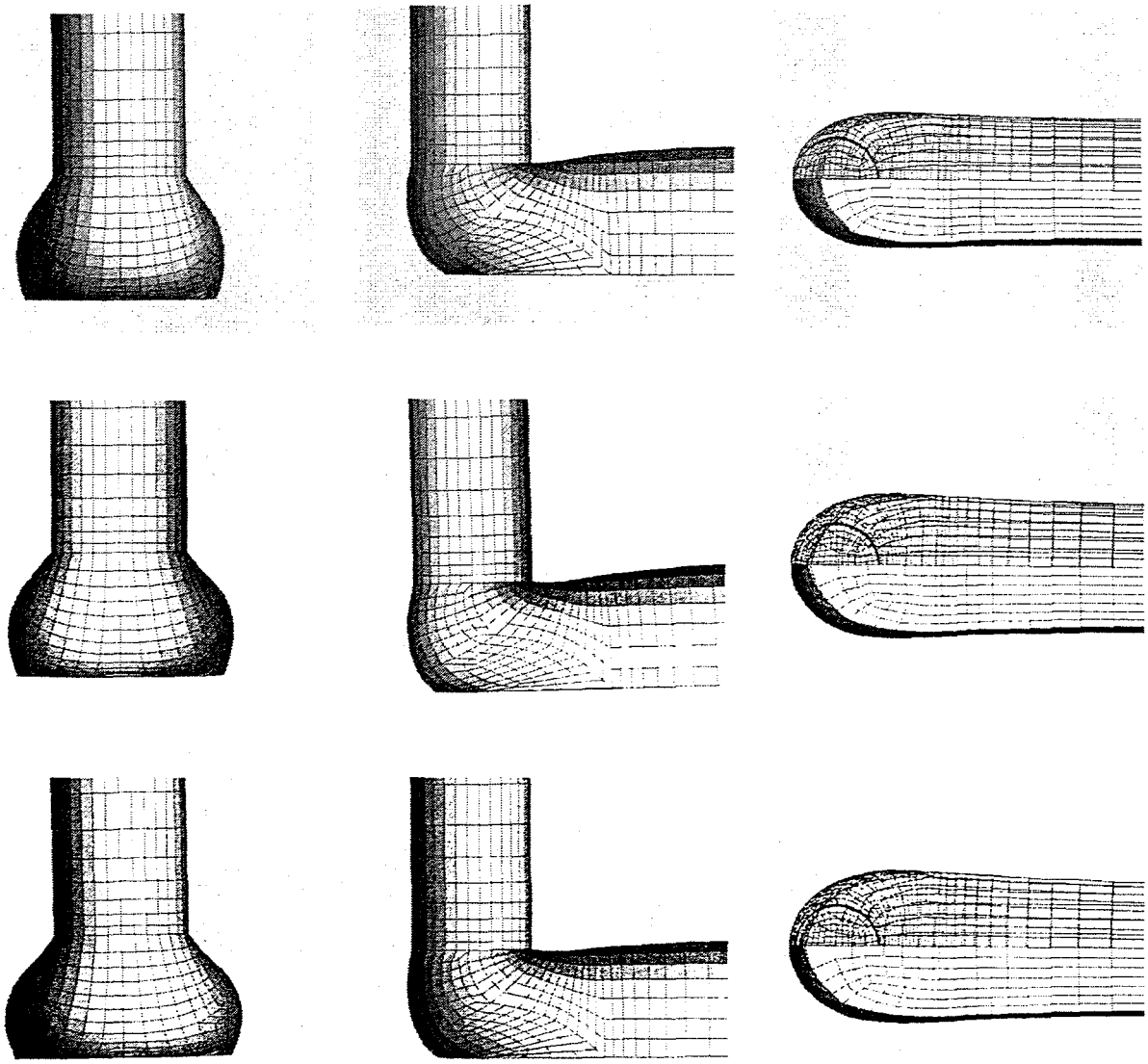

Figure 9 - Effect of surface tension on shape of bead laydown free surface shape. From top to bottom, global capillary numbers are 0.5, 1.0, 2.0. The inlet to web velocity ratio is 1.6.

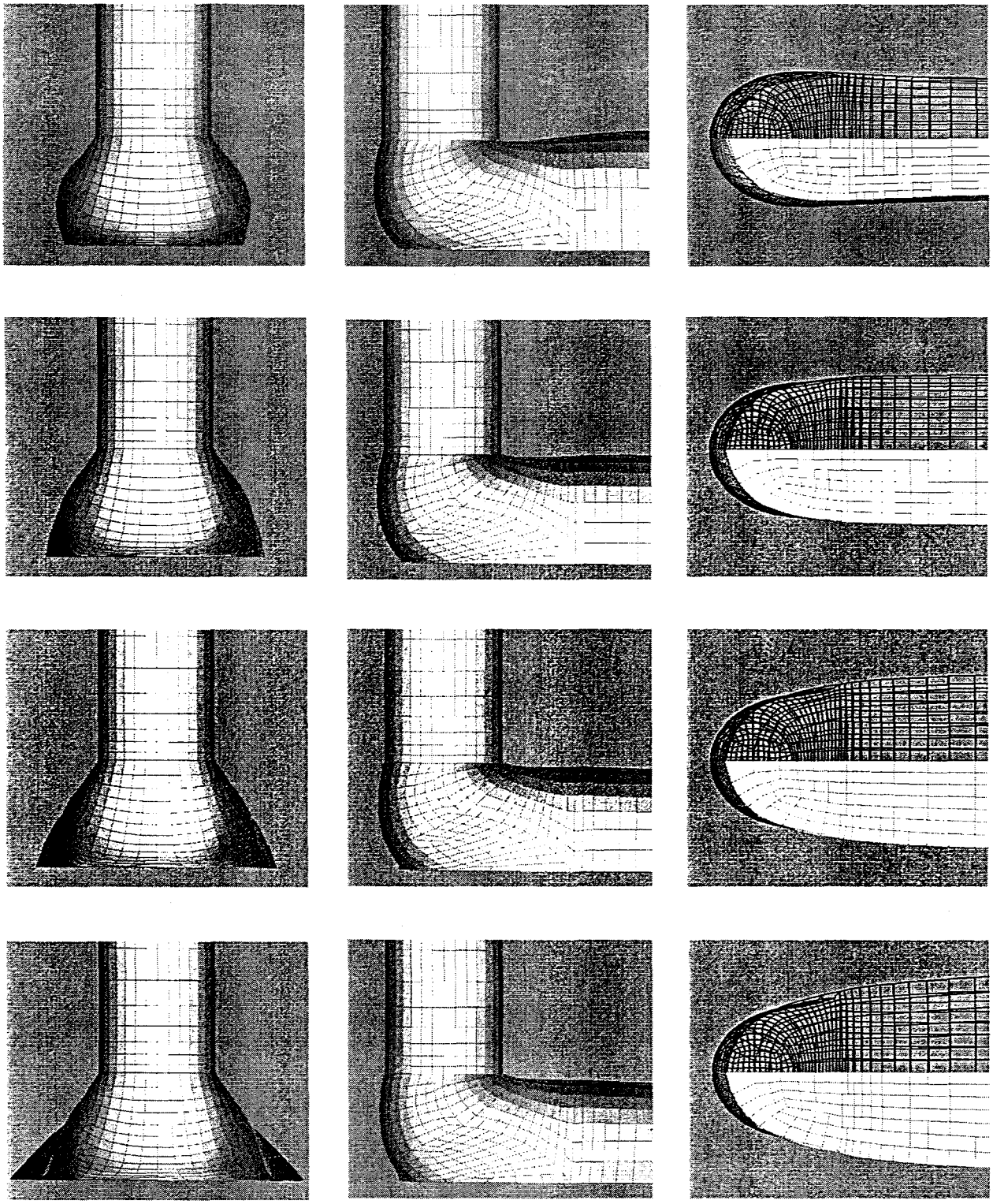

Figure 10 - Effect of static contact angle on shape of bead laydown free surface shape. From top to bottom, static contact angle values are 110°, 80°, 60°, and 45°. The inlet velocity to web velocity ratio is 1.6.

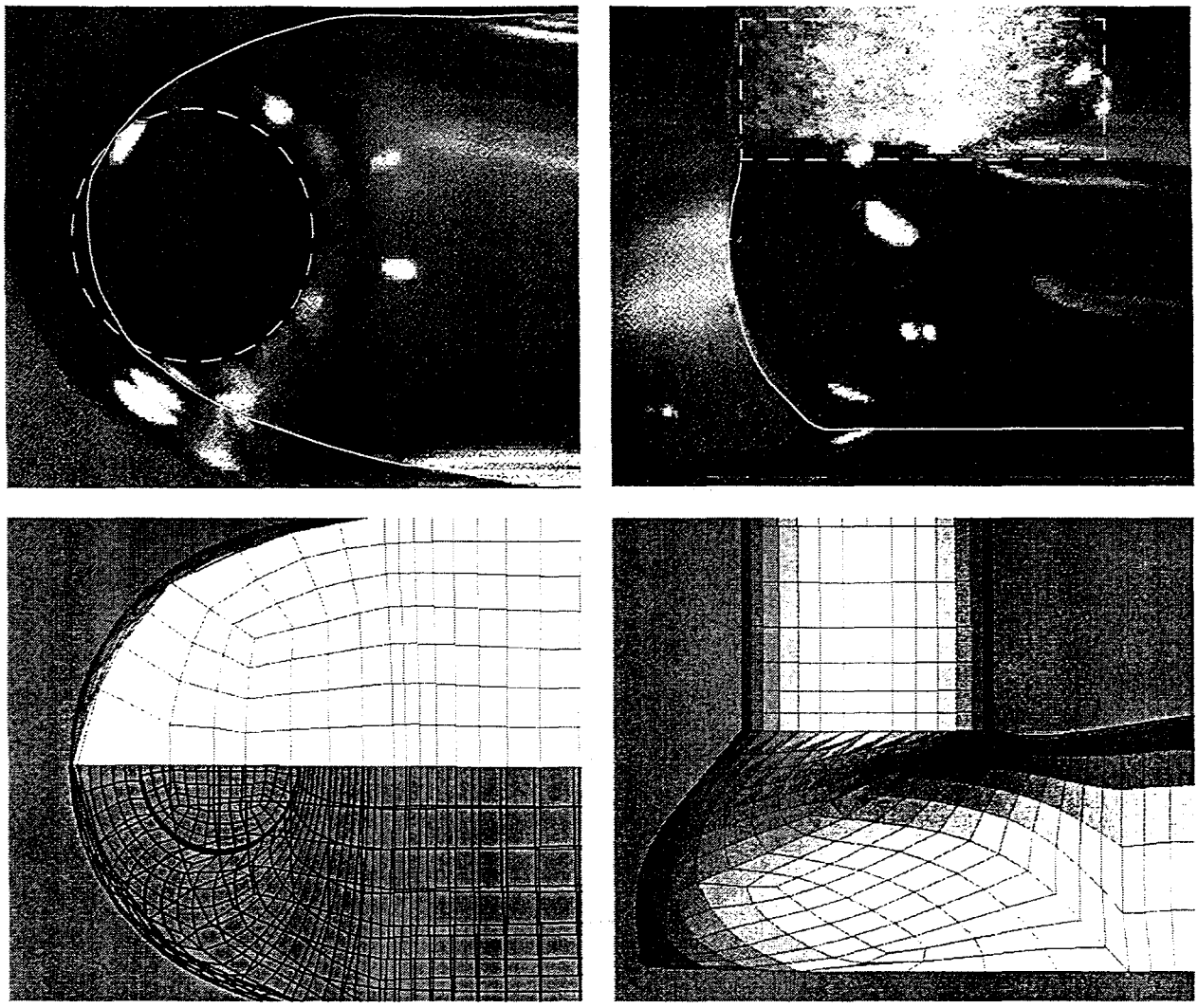

Figure 11 - Comparison of experimental visualization of bead laydown free surface shape (top line) and corresponding computed results (bottom line). Ratio of inlet average velocity to web speed: 3.2, global capillary number : 1.3. White line indicates location of free surface and/or dynamic contact line.

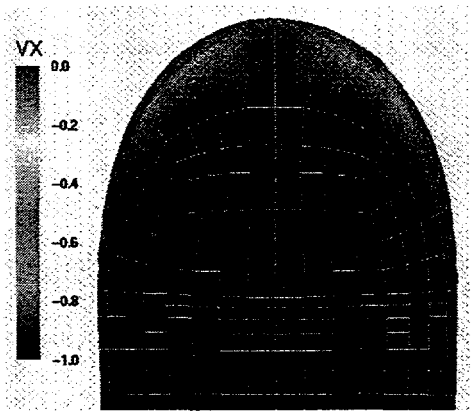

Figure 12 - Axial velocity component parallel to motion of web on interface plane between fluid and substrate. View is at the underside. Ratio of inlet average velocity to web speed: 3.2, global capillary number : 1.3.

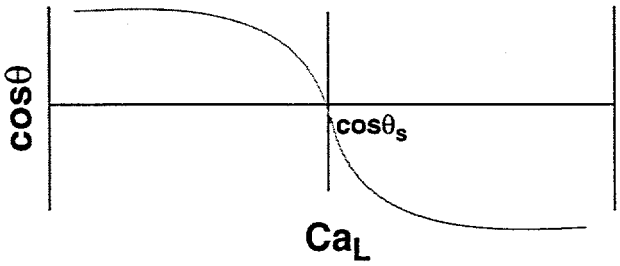

Figure 13 - Sketch of features that would be appropriate to a more physically accurate contact angle model.